Journal of the Mechanics and Physics of Solids 61 (2013) 472–488

Contents lists available at SciVerse ScienceDirect

Journal of the Mechanics and Physics of Solids

journal homepage: www.elsevier.com/locate/jmps

Prediction of fracture toughness of ceramic composites as function of microstructure: I. Numerical simulations

Yan Li [a], Min Zhou [a,b,*]

[a] The George W. Woodruff School of Mechanical Engineering, School of Materials Science and Engineering, Georgia Institute of Technology, Atlanta, GA 30332-0405, USA

[b] WCU Program on Multiscale Mechanical Design, School of Mechanical and Aerospace Engineering, Seoul National University, Seoul, Republic of Korea

ARTICLE INFO

Article history:
Received 14 February 2012
Received in revised form
12 August 2012
Accepted 11 September 2012
Available online 26 September 2012

Keywords:
Cohesive finite element method
Fracture toughness
Microstructure–fracture toughness relations
Weibull distribution

ABSTRACT

The evaluation of macroscopic material parameters such as fracture toughness as functions of microstructural attributes is a fundamental issue in material science. The task requires the quantification of both microstructure and material response. Currently, no systematic approach other than experiments exists for establishing microstructure–fracture toughness relations for materials. In this paper, we present a multi-scale computational framework based on the cohesive finite element method (CFEM) for predicting fracture toughness of materials as a function of microstructure. This framework provides a means for evaluating fracture toughness through explicit simulation of fracture processes in microstructures. The approach uses the *J*-integral, allowing fracture toughness to be calculated for microstructures with random heterogeneous phase distributions and fracture processes with arbitrary crack paths or microcrack patterns. Calculations carried out concern two-phase Al_2O_3/TiB_2 ceramic composites and focus on the effects of constitute behavior, phase morphology, phase distribution, phase size scale, and interphase bonding on fracture toughness. Results show that microstructure and constituent properties can significantly influence fracture behavior and combine to determine the overall fracture toughness through the activation of different fracture mechanisms. In particular, a combination of fine microstructure size scale, rounded reinforcement morphology, appropriately balanced interphase bonding strength and compliance can best promote desirable crack–reinforcement interactions and lead to enhanced fracture toughness.

1. Introduction

Microstructural constitutes, phase morphology and phase distribution can lead to significantly different fracture resistance values (Casellas et al., 2003; Curry and Knott, 1976; Hall et al., 1994). Microstructural design is an important approach for enhancing material behavior at the macroscopic scale. Tasks in this regard include proper characterization of microstructures and quantitative correlation of microstructural attributes with overall material response. Most analytical models allow the macroscopic response of materials to be estimated but yet do not allow the predictions of response that are unknown a priori. Such models usually require extensive experimental data to calibrate parameters that have little or no physical significance (Zohdi and Wriggers, 2008). Experimental studies can quantify macroscopic behavior and establish response–microstructure relations,

* Corresponding author at: The George W. Woodruff School of Mechanical Engineering, School of Materials Science and Engineering, Georgia Institute of Technology, Atlanta, GA 30332-0405, USA. Tel.: +1 404 894 3294; fax: +1 404 894 0186.
E-mail addresses: min.zhou@gatech.edu, min.zhou@me.gatech.edu (M. Zhou).

0022-5096/$ - see front matter © 2012 Elsevier Ltd. All rights reserved.
http://dx.doi.org/10.1016/j.jmps.2012.09.013

Nomenclature

A	area of reinforcement particle
C_l, C_s, C_r	longitudinal, shear and Rayleigh wave speeds
D	crack propagation distance
$d_{\max}$	maximum distance of a reinforcement particle
E_i	Young's modulus ($i=0$ or 1)
f	volume fraction
Φ	fracture energy
J	J-integral
K_i	bulk modulus ($i=0$ or 1)
K_{IC}^i	initiation fracture toughness
K_{IC}	propagation fracture toughness
K^0	normalization factor
K^L	lower bound fracture toughness
μ_i	shear modulus ($i=0$ or 1)
n	number of reinforcement particles
λ	state variable for interfacial separation
P_{ij}	two-point correlation functions ($i=0$ or 1; $j=0$ or 1)
$\overline{\rho}$	mean reinforcement particle roundness
$Q_1(Q_2)$	interfacial bonding strength ratio
R	particle radius
s	characteristic reinforcement size
$T_{\max}^{in}$	interfacial bonding strength
$T_{\max}^0$	baseline reference bonding strength
X	probability of fracture
Δ_{tc}	critical tangential separation
Δ_{nc}	critical normal separation
v	imposed boundary velocity
v_i	Poisson's ratio ($i=0$ or 1)
V	crack speed
W	strain energy density

but cannot be used to explore material configurations not yet in existence. The trial-and-error empirical approach for materials development is associated with high cost and long cycles. Computational modeling and simulation can provide an alternative and allow exploration of material configurations not yet in existence. Zhai et al. (2004) developed a computational framework that allows representation of material microstructure at different length scales and explicit account of different deformation and fracture mechanisms. Using this framework, we have developed an approach for evaluating the overall fracture toughness of materials based on a resolution of deformation and fracture processes at the microstructure level, accounting for microscopic heterogeneity and hierarchy. This approach uses the J-integral to quantify the fracture resistance as a function of microstructural attributes. Explicit tracking of fracture in the form of crack/microcrack initiation, propagation and coalescence and the evaluation of the J-integral throughout the fracture process allow the evolutions of the driving force for fracture and fracture resistance of the materials to be assessed. For brittle materials with linear elastic constituents, the overall fracture toughness K_{IC} of the material can be obtained through J for various material configurations, permitting microstructure–fracture toughness relations to be established.

The cohesive finite element method (CFEM) is employed to track fracture processes. Within this framework, two approaches exist for resolving fracture processes when crack paths are not known in advance. One is to insert cohesive elements ahead of the crack tip as crack develops (Pandolfi and Ortiz, 2002; Yu, 2001). This method can avoid cohesive-surface-induced stiffness reduction of the overall model when the traction–separation relation has finite initial stiffness. However, it is computationally expensive and requires specific fracture initiation criteria that are extrinsic to the overall finite element model. Another method entails embedding cohesive surfaces along all finite element boundaries as part of the physical model (Needleman, 1990; Xu and Needleman, 1985, 1994; Zhai et al., 2004). The cohesive surfaces permeate the whole microstructure as an intrinsic part of material characterization. Constitutive relations for the bulk phases and cohesive surfaces are specified separately. The cohesive relation allows damage and crack surface separation to be considered. Fracture emerges as a natural outcome of the deformation process without the use of any failure criterion. Although cohesive-surface-induced stiffness reduction is inevitable for this method if a cohesive relation with a finite initial stiffness is employed, proper choice of cohesive surface stiffness and finite element size (Tomar et al., 2004) can effectively alleviate and minimize its influence on computational results.

To characterize the microstructures analyzed, the two-point correlation functions (Berryman and Blair, 1986) are used. These functions allow attributes of microstructures such as the second-phase reinforcement size, volume fraction and spatial distribution to be readily extracted. The quantification is used to generate microstructural samples with independently varying characteristics so that the effect of each attribute on fracture toughness can be evaluated (Tewari et al., 2004). In addition, the two-point correlation functions provide a means to statistically parameterize the probability of crack interactions with these heterogeneities. This quantification lends itself to the establishment of relations between the statistical attributes of microstructure, fracture mechanism and the fracture toughness of the material. In addition to the two-point correlations functions which primarily characterize the distribution of phases and may be insensitive to the morphology of phases in a microstructure, our studies also reveal that additional descriptors or parameters quantifying the morphology of phases are needed to sufficiently quantify and distinguish between different microstructures with varying reinforcement sizes and shapes. The influence of such a parameter (i.e., the roundness of reinforcement particles) on the fracture toughness is also discussed.

Besides the geometric attributes of the microstructure, the constituent properties also greatly influence the overall fracture toughness. Specifically, the effects of the toughness of second-phase reinforcement and interfacial bonding characteristics are also analyzed through systematic variations of relevant parameters.

Although the framework developed here can be applied to any material system in principle, computations in this paper concern Al_2O_3/TiB_2 ceramic composites. These two-phase materials consist of an Al_2O_3 matrix and a TiB_2 reinforcement phase. Microstructures with more than two phases can also be analyzed. Based on the numerical results, relations between microstrucutral parameters and fracture toughness are established. These relations can be used for the selection of materials and the design of new materials with tailored properties.

2. CFEM-based multi-scale framework

Models at the macrostructural scale cannot account for material heterogeneity at the microstructural scale. The use of homogenized material properties yields results that do not reflect stochastic variations of material behavior which is intrinsic at the microstructural level. Such models cannot and do not attempt to explain the statistical variation in quantities such as K_{IC} (Wallin, 1984). On the other hand, models at the microstructual scale account for material heterogeneity and resolve different deformation and failure mechanisms. Such models have fine resolutions and, as a result, are computationally intensive and are impractical for use at the structural scale.

A framework that combines both scales can overcome the shortcomings of each type of models. For example, the configuration illustrated in Fig. 1 allows explicit representation of microstructures and account of microstructural level of deformation, damage and failure mechanisms, while allowing macroscopic conditions such as controlled loading and structural response to be considered at the same time. This framework provides a means for calibrating model parameters at the microscale through macroscale responses which can be easily measured in experiments. More importantly, it allows macroscopic response measures such as K_{IC} to be evaluated as functions of microstructure by calculating the J-integral along an arbitrary contour within the homogenized region, as indicated by the dashed lines in Fig. 1.

The edge-cracked square specimen under Mode I tensile loading in Fig. 1 has a size length of 3.65 mm. The microstructure region has a length of 2 mm, width of 1 mm and a pre-crack length of 0.73 mm. A boundary velocity between $v = 5\times10^{-4}$ mm/s and $v = 15$ mm/s is imposed at the top and bottom edges to effect tensile loading. The remaining edges of the specimen are traction-free. Conditions of plain strain are assumed to prevail.

2.1. Constitutive behavior of constituents

Both the Al_2O_3 and TiB_2 phases in the composites follow isotropic linear elastic constitutive relations. Specifically, the constitutive law is

$$\boldsymbol{\sigma} = \frac{E}{1+v}\boldsymbol{\varepsilon} + \frac{vE}{(1+v)(1-2v)}tr(\boldsymbol{\varepsilon})\boldsymbol{I}, \tag{1}$$

where $\boldsymbol{\sigma}$ and $\boldsymbol{\varepsilon}$ are the stress and strain, respectively, E is Young's modulus. v is Poisson's ratio, tr($\boldsymbol{\varepsilon}$) is the trace of $\boldsymbol{\varepsilon}$ and $\boldsymbol{I}$ is the second order identity tensor. The values of the material constants for the constituents are summarized in Table 1.

2.2. Constitutive behavior of interfaces

The interface between the constituents and all potential crack faces within each constituent are assigned a constitutive law for cohesive surfaces. This interfacial constitutive law takes the form of a bilinear relation between traction and interfacial separation, as illustrated in Fig. 2. The bilinear law used can be regarded as a generalized version of those with

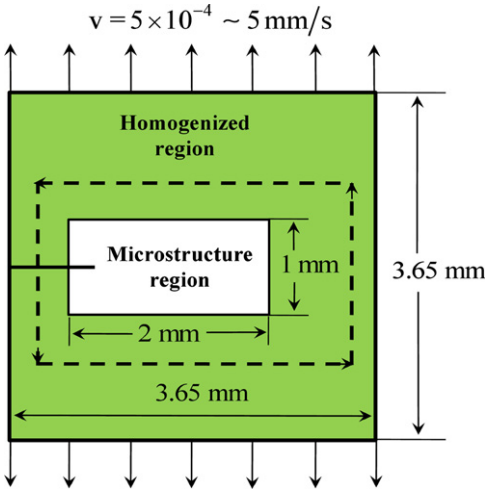

Fig. 1. Specimen configuration used in the analysis.

Table 1
Constitutive parameters for bulk constituents and cohesive surfaces.

Compound	Density (kg/m^3)	K_{IC} (MPa$\sqrt{\text{m}}$)	E (GPa)	ν	$T_{\max}$ (GPa)	Δ_{tc}, Δ_{nc} (nm)	Φ (J/m^2)
Al_2O_3	3990	2.7	340	0.23	0.48	90	21.5
TiB_2	4520	7.2	500	0.12	0.70	292	102.2
Interface					0.60	262	78.5

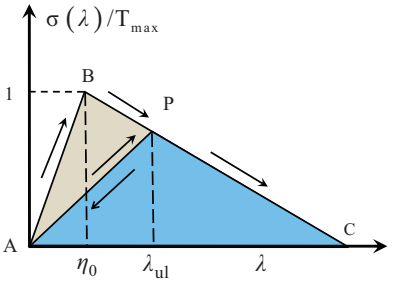

Fig. 2. Bilinear traction–separation law.

irreversibility given by Camacho and Ortiz (1996) and Ortiz and Pandolfi (1999). However, as in Espinosa et al. (2000), additional parameters are needed to define the finite initial stiffness of the cohesive surfaces and the irreversibility of separation with damage. This law is derived from a potential Φ which is a function of separation vector Δ through a state variable defined as $\lambda=\sqrt{(\Delta_n/\Delta_{nc})^2+(\Delta_t/\Delta_{tc})^2}$. This variable describes the effective instantaneous state of mixed-mode separations. Here, $\Delta_n=n\cdot\Delta$ and $\Delta_t=t\cdot\Delta$ denote, respectively, the normal and tangential components of $\boldsymbol{\Delta}$, with $\mathbf{n}$ and $\mathbf{t}$ being unit normal and tangent vectors. Δ_{nc} is the critical normal separation at which the cohesive strength of an interface vanishes under conditions of pure normal deformation ($\Delta_t=0$). Similarly, Δ_{tc} is the critical tangential separation at which the cohesive strength of an interface vanishes under conditions of pure shear deformation ($\Delta_n=0$). λ tracks instantaneous mixed-mode separations during both loading and unloading. Apparently, $\lambda=0$ corresponds to $\Delta=0$ (undeformed state or fully unloaded state) and $\lambda\geq 1$ implies complete separation, i.e. total debonding of the cohesive surface pair.

A parameter $\eta=\max\{\eta_0,\lambda_{ul}\}$ is defined to account for the irreversibility of surface separations. As illustrated in Fig. 2, η_0 is the initial value of η which defines the stiffness of the original undamaged cohesive surface and λ_{ul} is the hitherto maximum value of λ at which an unloading process was initiated.

The specific expression for potential s is of the form

$$\Phi=\Phi(\lambda,\eta)=\begin{cases}\Phi_0\left(\frac{1-\eta}{1-\eta_o}\right)\left(\frac{\lambda^2}{\eta}\right), & \text{if } 0\leq\lambda\leq\eta,\\ \Phi_0\left(\frac{1-\eta}{1-\eta_o}\right)\left(1-\frac{(1-\lambda)^2}{1-\eta}\right), & \text{if } \eta\leq\lambda\leq 1,\\ 0, \quad \textit{if } \lambda>1.\end{cases} \tag{2}$$

Based on the above relation, the traction is defined as

$$\begin{cases}T_n=\sigma(\lambda,\eta)\frac{\Delta_n}{\lambda\partial\Delta_{nc}} & \text{and}\\ T_t=\sigma(\lambda,\eta)\frac{\alpha\Delta_t}{\lambda\partial\Delta_{tc}},\end{cases} \tag{3}$$

yielding the normal and shear traction components as

$$T=\frac{\partial\Phi}{\partial\Delta} \tag{4}$$

with

$$\alpha=\frac{\Delta_{nc}}{\Delta_{tc}}. \tag{5}$$

Therefore,

$$\sigma=\begin{cases}\left(T_{\max}\frac{1-\eta}{1-\eta_o}\right)\left(\frac{\lambda}{\eta}\right), & \text{if } 0\leq\lambda\leq\eta,\\ \left(T_{\max}\frac{1-\eta}{1-\eta_o}\right)\left(\frac{1-\lambda}{1-\eta}\right), & \text{if } \eta\leq\lambda\leq 1,\\ 0, \quad \textit{if}\lambda>1.\end{cases} \tag{6}$$

The work per unit interface area for an arbitrary separation process is

$$\int_0^{\Delta_c} \mathrm{T}\cdot d\Delta = \Phi(1,\eta) = \frac{1}{2}T_n^{\max}\Delta_{nc} = \frac{1}{2}\alpha T_t^{\max}\Delta_{tc}. \tag{7}$$

CFEM models with cohesive traction–separation laws with finite initial stiffness have two competing requirements on element size. The upper bound requires that the element size must be small enough to accurately resolve the stress distribution inside the cohesive zones at crack tips. The lower bound, on the other side, requires the cohesive surface induced stiffness reduction be small, such that the wave speed in the solid is not significantly affected due to the presence of the cohesive surfaces. For the conditions of this paper, the preferred range of the element size is $7\ \mu\mathrm{m} \ll h \ll 14\ \mu\mathrm{m}$, allowing the convergence criterion in Tomar et al. (2004) to be satisfied.

2.3. Model structure

The parameters for the bilinear cohesive law are chosen such that the work of separation matches experimentally measured fracture toughness values for the corresponding constituent. For Al_2O_3/TiB_2 composites, three types of cohesive elements exist: Al_2O_3–Al_2O_3, TiB_2–TiB_2 and Al_2O_3–TiB_2. Xu and Needleman (1994) suggested that the maximum traction $T_{\max}$ should be between $E/100$ and $E/200$. Therefore, Δ_{nc} and Δ_{tc} can be determined from Eq. (7). For linear elastic materials, $\Phi = G_{IC} = J_{IC} = [(1-\nu^2)/E]K_{IC}$, where K_{IC} is the fracture toughness of the material in question. According to the experimental results reported by Logan (1996) and Wiederhorn (1984), the K_{IC} values of the matrix Al_2O_3 and the reinforcement TiB_2 are chosen as $2.7\mathrm{MPa}\sqrt{\mathrm{m}}$ and $7.2\mathrm{MPa}\sqrt{\mathrm{m}}$, respectively. The cohesive strength $T_{\max}$ for each phase is calibrated accordingly to satisfy the fracture toughness of the single phase. Since the experimental K_{IC} value for the interface is not yet available in the current literature, its cohesive strength $T_{\max}$ is considered as the average value of the matrix and reinforcement cohesive strength in this paper. All the constitutive parameters for the bulk constituents and cohesive surfaces are listed in Table 1.

The effective properties for the homogenized region are estimated by using the Mori–Tanaka method. Specifically, the effective bulk and shear moduli are

$$\begin{cases} \overline{K} = K_0 + \dfrac{f(K_1-K_0)(3K_0+4\mu_0)}{3K_0+4\mu_0+3(1-f)(K_1-K_0)} & \text{and} \\ \overline{\mu} = \mu_0 + \dfrac{5f\mu_0(\mu_1-\mu_0)(3K_0+4\mu_0)}{5\mu_0(3K_0+4\mu_0)+6(1-f)(\mu_1-\mu_0)(K_0+2\mu_0)} & \end{cases}. \tag{8}$$

Here, f is the volume fraction of the TiB_2 phase, K_r and μ_r are the bulk and shear modulus, respectively for Al_2O_3 ($r=0$) and TiB_2 ($r=1$).

The effective Young's modulus $\overline{\rho}$ and Poisson's ratio s for the homogenized region are, respectively,

$$\begin{cases} \overline{E} = \dfrac{9\overline{K}\overline{\mu}}{3\overline{K}+\overline{\mu}} & \text{and} \\ \overline{\nu} = \dfrac{3\overline{K}-2\overline{\mu}}{6\overline{K}+2\overline{\mu}}. & \end{cases} \tag{9}$$

The variations of $\overline{E}$ and $\overline{\nu}$ as functions of f are illustrated in Fig. 3.

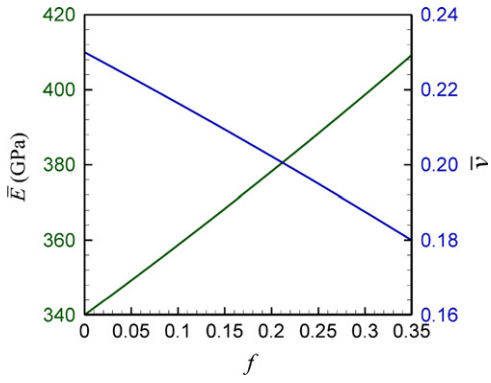

Fig. 3. Homogenized material properties at different TiB_2 volume fractions.

3. *J*-integral-based fracture toughness evaluation

The TiB_2 and Al_2O_3 phases are assumed to be isotropic and linear elastic. For this type of material, the longitudinal, shear and Rayleigh wave speeds are (Freund, 1998) as follows:

$$C_l=\sqrt{\frac{\overline{E}(1-\overline{v})}{\overline{\rho}(1+\overline{v})(1-2\overline{v})}},\quad C_s=\sqrt{\frac{\overline{E}}{2\overline{\rho}(1+\overline{v})}},\quad C_r=C_s\frac{0.862+1.14\overline{v}}{1+\overline{v}}. \tag{10}$$

Here, $\overline{\rho}=4200\ \mathrm{kg}/m^3$ is taken as the homogenized material density. $\overline{E}$ and $\overline{v}$ are calculated according to Eq. (9). Therefore, the longitudinal, shear and Rayleigh wave speeds are in the range of [9688, 10286] m/s, [5737, 6426] m/s and [5243, 5812] m/s, respectively. The *J*-integral is equivalent to the energy release rate *G* and can be related to the stress intensity factor *K* via (Anderson, 1995) the following:

$$K^2=\frac{J}{A(V)}\frac{E}{1-v^2}, \tag{11}$$

where *V* is the crack speed and $A(V)=V^2\beta_1/(1-v)C_s^2D$ with $\beta_1=\sqrt{1-(V/C_l)^2}$, $\beta_2=\sqrt{1-(V/C_s)^2}$ and $D=4\beta_1\beta_2-(1+\beta_2^2)^2$. Note that as $V\to 0$, $A(V)\to 1$.

Crack propagation can be dynamic even under quasistatic loading (Duffy et al., 1988; Toshiro et al., 1988). To account for inertia effects, a fully dynamic deformation formulation is used. Within this framework, the path-independent *J*-integral is (Lo and Nakamura, 1993; Moran and Shih, 1987; Nakamura et al., 1985) as follows:

$$J=\int_\Gamma\left[\left(\int_0^t\boldsymbol{\sigma}:d\boldsymbol{\varepsilon}+\frac{1}{2}\rho\dot{\mathbf{u}}\cdot\dot{\mathbf{u}}\right)dx_2-\mathbf{t}\cdot\frac{\partial\mathbf{u}}{\partial x_1}ds\right]+\int_A\left(\rho\ddot{\mathbf{u}}\cdot\frac{\partial\mathbf{u}}{\partial x_1}-\rho\dot{\mathbf{u}}\cdot\frac{\partial\dot{\mathbf{u}}}{\partial x_1}\right)dA, \tag{12}$$

where $\mathbf{t}$ is the traction on a surface with normal $\mathbf{N}$, $\mathbf{u}$ is the displacement, $\boldsymbol{\varepsilon}$ denotes the strain and ρ is the mass density.

For the model shown in Fig. 1, contours for *J* evaluation are solely within the homogenized part of the specimen where no cohesive elements are used. Due to the path-independent property of *J*-integral, the results extracted from different contours are very close to each other. In the remainder of this paper, we will use the average value of *J* from four different contours in order to best eliminate numerical error.

For steady state crack growth, the driving force represented by *J* balances out the fracture resistance, allowing the fracture resistance to be evaluated through Eq. (11). To calculate *J* and in turn *K*, boundary velocities between 5×10^{-4} mm/s and 15 mm/s are applied. The results for a microstructure with circular reinforcement particles are shown in Fig. 4. Fig. 4(a) shows $J/A(V)$ as a function of crack length and Fig. 4(b) illustrates the corresponding histories of crack speed. Reflecting the wide range of boundary loading velocities, the crack speeds for the different cases span from approximately 28 m/s for $v=5\times10^{-4}$ mm/s, 392 m/s for $v=5\times10^{-3}$ mm/s, 1295 m/s for $v=5\times10^{-2}$ mm/s to approximately 3600 m/s for $v>0.5$ mm/s. The highest value is approximately 60% of the Rayleigh wave speed of the composite. Upon the arrival of the loading wave at the crack tip region, the $J/A(V)$ starts to increase rapidly. When the value reaches point A, the crack begins to propagate slowly and steadily (crack speed below 25 m/s). At point B, both $J/A(V)$ and the crack speed increase rapidly and quickly reach point C. Beyond point C, the crack speed oscillates around an average value as the crack encounters and passes reinforcement particles. Although the instantaneous crack speed is not steady over short distances, the average crack speed is quite steady over longer distances between points C and D. Also, at the lower crack speeds the magnitudes of the oscillations in both the crack speed and $J/A(V)$ are lower. At the lowest speed of approximately 28 m/s, the oscillation is the lowest and the propagation of the crack can be approximately regarded as quasistatic. The time it takes for stress waves to traverse the distance between the crack tip and the boundary of the specimen is approximately 0.2 μs. In contrast, time interval for crack propagation is approximately 149.6 μs. This

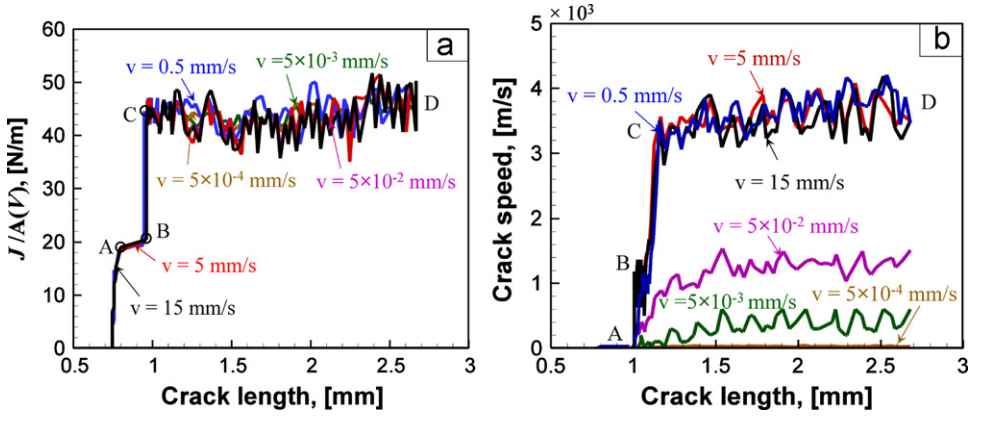

Fig. 4. (a) Comparison of $J/A(V)$ under different loading rates, (b) Comparison of crack speed under different loading rates.

specimen design allows the calculations to approximate conditions of quasi-static loading. It is important to note that $J|A(V)$ for all the cases essentially coincide, even though the crack speed spans three orders of magnitude. This is expected as the brittle ceramic system considered here is rate-independent. This observation suggests that the fracture toughness values obtained may be regarded as both quasistatic and dynamic, within the fully elastic material constitutive framework considered here. Since all loading velocities give consistent results, unless otherwise noted most calculations in this paper are carried out with $v = 5$ mm/s for computational efficiency.

The fracture toughness of composites may not be sufficiently captured by a single parameter, as argued by Manoharan and Kamat (1993). The issue is even more pronounced for processes of crack initiation and propagation. Here, we measure both the initiation toughness K_{IC}^{i} and the propagation toughness K_{IC} from the evolution of J. The initiation toughness is measured at the critical point where the crack begins to propagate [point A, Fig. 4(a)]. The propagation toughness is obtained from the average J value over the distance the crack traverses a sufficiently representative part of the microstructure, between points C and D in Fig. 4(a).

To illustrate the fracture process studied, Fig. 5 shows six snap shots of the crack propagation process in a microstructure with circular TiB_2 reinforcement at a loading velocity of $v = 5$ mm/s. The corresponding histories of J and K are shown in Fig. 6. Fracture initiates in the Al_2O_3 matrix at 105.0 μs [Fig. 5(a)], this event defines the initiation

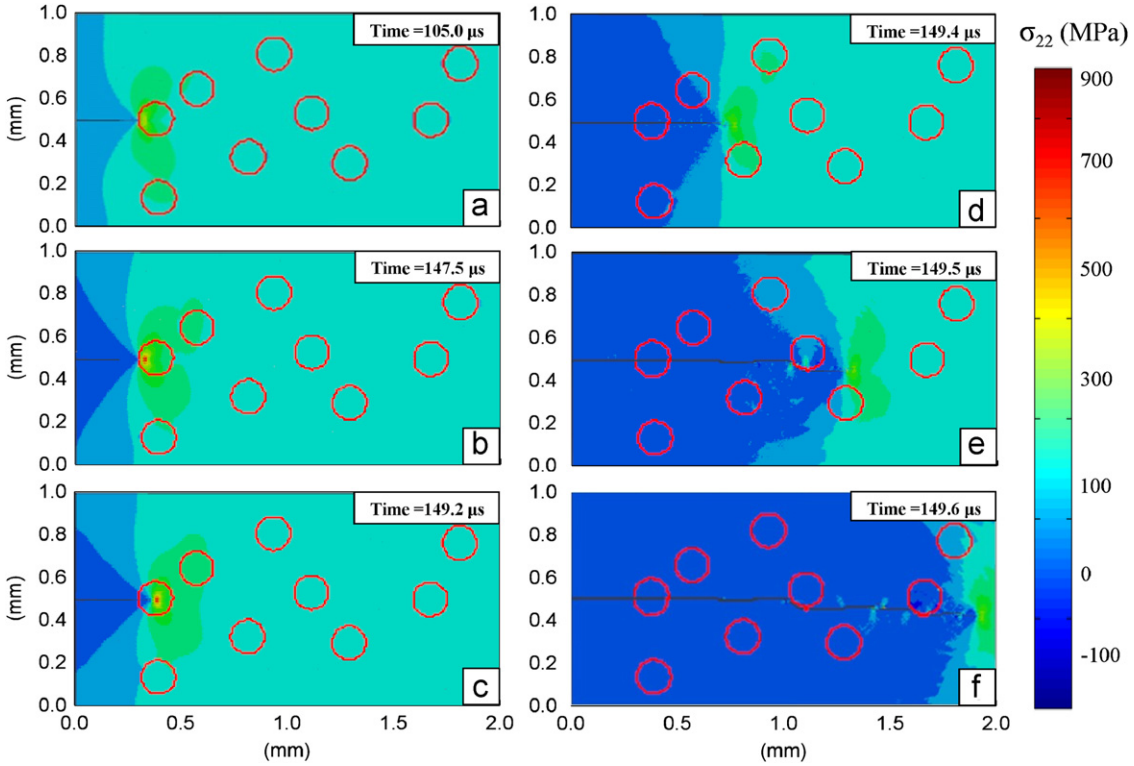

Fig. 5. Crack propagation in a microstructure with circular reinforcement.

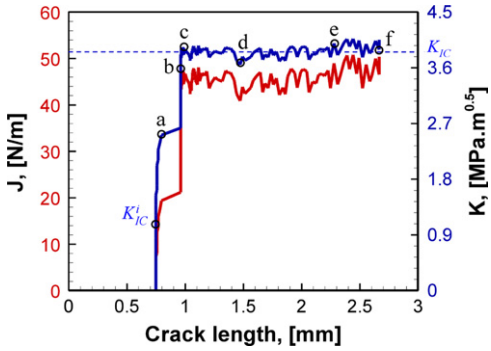

Fig. 6. Evolution of J and K during the crack propagation process in Fig. 5.

toughness K_{IC}^{i}. The crack is arrested by a TiB_2 particle and pauses at the Al_2O_3/TiB_2 interface for approximately 42.5 μs [Fig. 5(b)]. During the pause, J increases rapidly. At approximately 149.2 μs [Fig. 5(c)], as a result of the higher level of driving force J, the crack penetrates the TiB_2 particle. Subsequently, the crack propagates rapidly, causing J (and therefore K) to plateau for the remainder of the analysis. The average value of K during this period is taken as the propagation toughness K_{IC}.

4. Results and discussion

Microstructure and constituent properties determine the overall fracture behavior through the activation of different fracture mechanisms, including matrix cracking, interface debonding and particle cracking. Real microstructures with stochastic distributions of phases and computationally generated microstructures with systematically and independently varying attributes are quantified and used in the analysis. Both sets of microstructure samples are illustrated in Figs. 7 and 8. We will first discuss the effects of microstructure on fracture toughness and then discuss the effects of constituent properties.

4.1. Statistical characterization of microstructure

Microstructural attributes such as reinforcement size, reinforcement volume fraction, reinforcement morphology, and distributions of the phases significantly influence the material behavior and are, therefore, of primary consideration in material design. To provide a characterization of the microstructures in the context of fracture analysis, we consider the two-point correlation functions which are often used to quantify microstructures (Tewari et al., 2004; Torquato and Haslach, 2002). The functions measure the probability of finding a given combination of phases over given distances. Specifically, in 2D microstructures with two phases such as the one shown in Fig. 9, the function P_{ij} denotes the probability for randomly placed vectors of a given length to start in phase i ($i=0$ or 1) and ends in phase j(0 or 1). It is noticed that only three of the four two-point correlation functions are independent since $P_{00}+P_{01}+P_{10}+P_{11}=1$. In this paper, the matrix is defined as phase 0, and the reinforcement is defined as phase 1. f Denotes the volume fraction of the reinforcement phase.

Fig. 10(a) shows the two-point correlation representation (P_{01}) of a set of microstructures with randomly distributed uniform circular particles. The peak of each curve occurs at a distance equal to the particle diameter as shown in the inset. The two-point correlation functions can be quantified by the following functions:

$$\begin{cases} P_{11}=(f-f^2)e^{-(D/s)}+f^2, \\ P_{00}=[(1-f)-(1-f)^2]e^{-(D/s)}+(1-f)^2, \ \textit{and} \\ P_{01}=P_{10}=(1-P_{11}-P_{00})/2. \end{cases} \tag{13}$$

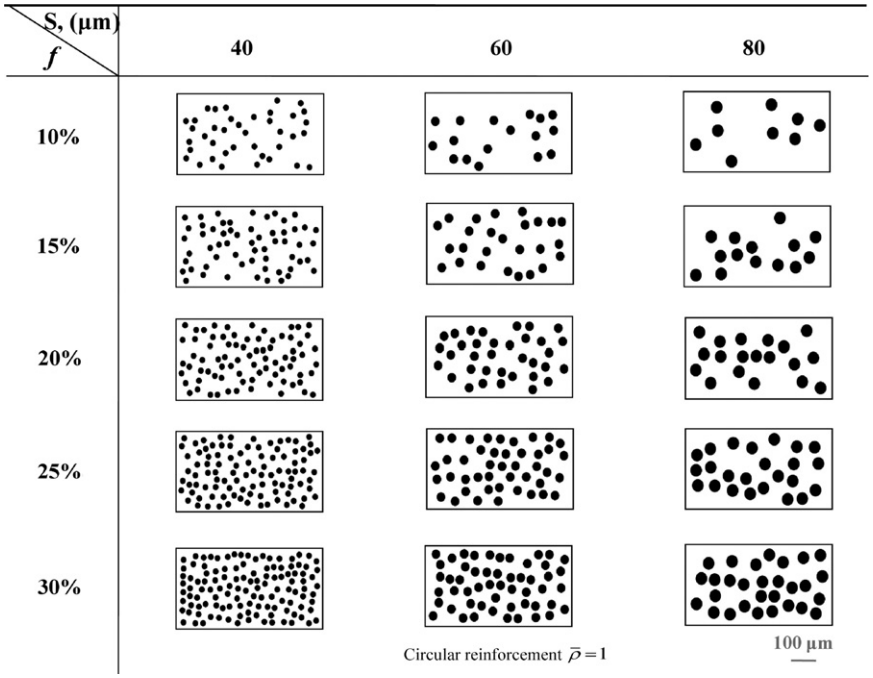

Fig. 7. Design space of microstructures with randomly distributed, non-overlapping circular reinforcements. Twenty random instantiations (samples) of each microstructure are used in the calculations to obtain a statistical characterization of the result for each case. * f is the reinforcement volume fraction. s and $\bar{\rho}$ are characteristic reinforcement size and roundness, respectively, as defined in Section 4.1.

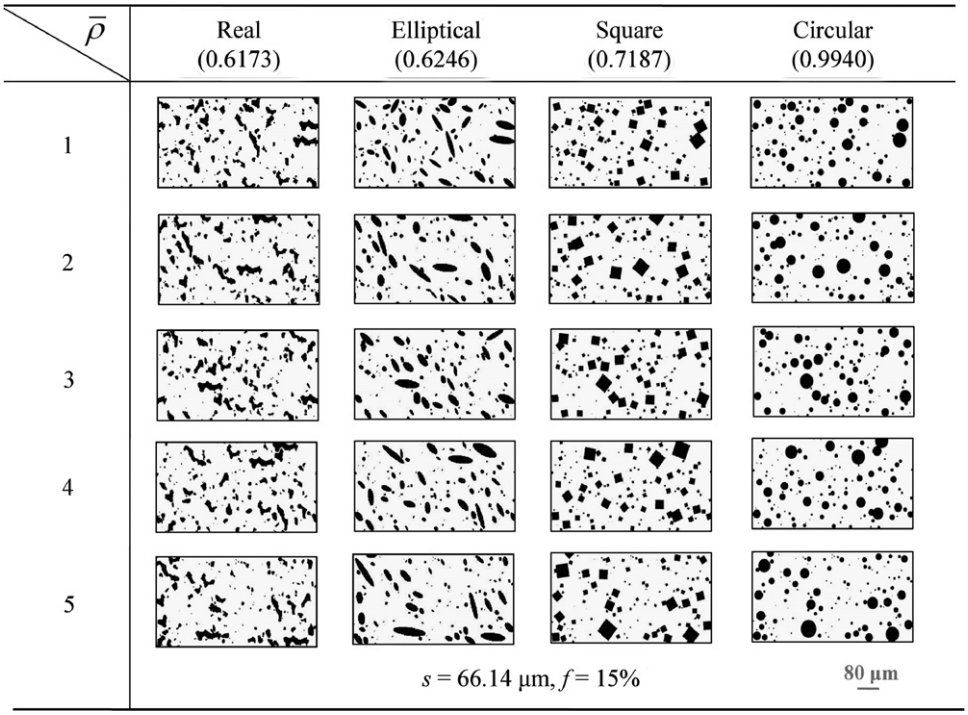

Fig. 8. Design space of microstructures with various reinforcement shapes. Twenty random instantiations (samples) of each microstructure are used in the calculations to obtain a statistical characterization of the result for each case. * f is the reinforcement volume fraction. s and $\overline{\rho}$ are characteristic reinforcement size and roundness, respectively, as defined in Section 4.1.

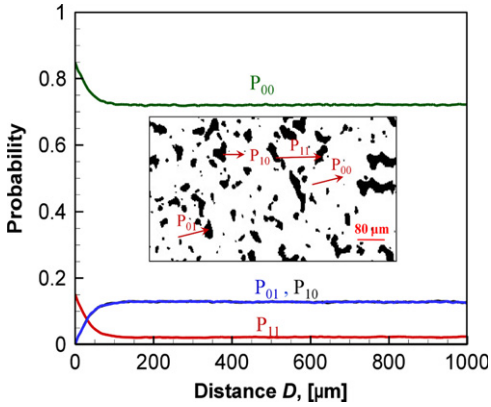

Fig. 9. Two-point correlation function for a two-phase microstructure.

Here, s is a parameter representing the characteristic size of the reinforcement. For microstructures with randomly distributed circular particles of the same diameter, s is equal to the diameter. P_{01} can be regarded as the geometric probability of encountering the reinforcement phase by a crack of a certain length that is propagating in the matrix. The area underneath the P_{01} curve, which is denoted as F_{01} in Fig. 10(b), can be taken as a measure for the cumulative interactions with the reinforcement phase by a straight crack over its course of propagation. Obviously, F_{01} becomes linear beyond a certain distance (D_{cha}) at which P_{01} reaches its long-distance limit of $[1-f^2-(1-f)^2]/2$. This distance (D_{cha}) is taken as a characteristic length for the microstructure. For crack lengths below D_{cha}, the probabilistic interactions of a crack with the reinforcement phase sensitively depends on not only the volume fraction of the reinforcement, but also the phase morphology and phase size scale. Beyond D_{cha}, the long-term geometric probability of a straight crack encountering the reinforcement phase depends only on the volume fraction of the reinforcement (since the values of P_{ij} beyond D_{cha} depends only on f), not phase morphology or size scale. Naturally, to sufficiently capture the fracture behavior of different macrostructures, crack propagations over distances longer than the characteristic lengths of the microstructures must be considered. In the analyses carried out here, the characteristics lengths of the microstructures are less than 100 μm and

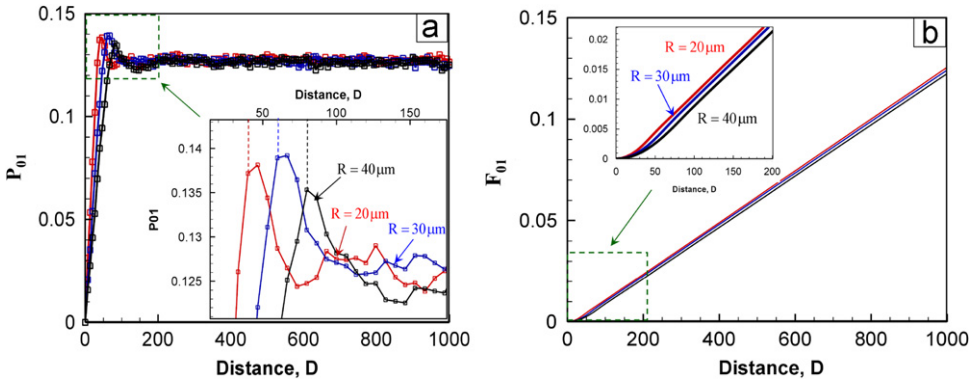

Fig. 10. (a) Interpretation of P_{01} and (b) F_{01}.

the total distances of crack propagation are 1.5–2 mm. To compare the propagation toughness of different microstructures, the F_{01} values at the same crack propagation distance of 800 μm are used.

4.2. Correlation between fracture toughness and microstructural attributes

Microstructural sample set 1, as listed in Fig. 7, is employed to study the correlations between the two-point correlation parameter F_{01} and fracture toughness. Note that this set has systematically varying particle radius ($R = s/2 = 20$ μm, 30 μm and 40 μm) and volume fraction ($f = 10\%$, 15%, 20% and 25%). For each combination of particle size and volume fraction, 20 randomly generated microstructural instantiations are used to obtain a statistical characterization of the stochastic nature of the failure processes at the microstructure level. For each microstructure setting (each combination of R and f), the probability of fracture initiation is measured in terms of K_{IC}^{i} and the probability of catastrophic fracture is measured by the propagation toughness K_{IC}. Both measurements are through the three-parameter Weibull distribution function (Weibull, 1939) in the form of

$$X(K) = 1 - e^{-\Phi(K)}, \text{ where } \Phi(K) = \begin{cases} \left(\frac{K-K^L}{K^0}\right)^m, & K^L \le K < \infty; \\ 0, & 0 \le K \le K^L. \end{cases} \tag{14}$$

Here, X is the probability of fracture, K can be either the initiation toughness K_{IC}^{i} or propagation toughness K_{IC}, m quantifies the scatter of K, K^L is the lower bound fracture toughness and K^0 is the normalization factor. The parameters K^L, K^0 and m are obtained through a linear regression fit to the 20 data points for each microstructural setting which involves 20 different instantiations.

The Weibull distribution function has been widely used in reliability analysis due to its versatility and relative simplicity (Doig, 1985; Wallin, 1993; Wallin et al., 1992). The shape (defined by m), size (defined by K^0) and finite lower bound limit (at $W(K) = 95\%$) of the curve make it a better representation of fracture toughness distribution than the normal distribution function whose symmetry about the mean can result in physically unrealistic predictions of the lower bound values (Wallin, 1984).

As shown in Fig. 11, microstructure affects K_{IC} much more than K_{IC}^{i}. The finest reinforcements give rise to the highest propagation toughness, but have the least influence on the initiation toughness. The opposite trends in influence have to do with how cracks interact with particles. If a large particle happens to be at the tip of the pre-crack, a higher level of stress is required to initiate the crack and, consequently, the initiation toughness is higher. Such events are less frequent, as shown in Fig. 11. On the other hand, a propagating crack is more likely to penetrate a large particle, causing immediate catastrophic failure of the material and limited improvement of the propagation toughness.

It is worth noting in Fig. 12 that the K_{IC} range obtained from the CFEM framework is in good agreement with the experimental results reported by Logan (1996) which are also shown. Increasing the reinforcement volume fraction f always enhances K_{IC}^{i}, but does not always enhance K_{IC}. As shown in Fig. 12, K_{IC} decreases as f increases when the particles are large ($R = 40$ μm). At $R = 30$ μm, K_{IC} is the highest for $f = 20\%$ and is lower at both $f = 10\%$ and $f = 30\%$. The effect of f becomes less pronounced when R is further decreased to 20 μm. The above trends are result from relative shifts in the three fracture mechanisms (matrix cracking, interface debonding and particle cracking) as the microstructure changes. Specifically, it has been reported that particle cracking is more prevalent in composites with higher particle volume fractions (Kumai et al., 1991). The lower fracture toughness values at larger particle sizes are a result of an increased likelihood of particle cracking (Evans, 1990; Lin et al., 1986). Although crack penetration through a particle requires a higher instantaneous K value than crack growth through interfacial debonding, particle cracking usually signifies immediate catastrophic failure. Small particles, on the other hand, promote sustained crack deflections through interfacial debonding as illustrated in Fig. 13. Such processes increase the tortuosity of crack trajectory and in turn enhance the fracture resistance.

As discussed above, the fracture toughness of a material is not a deterministic quantity even if the microstructure contains uniformly distributed reinforcement particles of the same radius (Kobayashi et al., 1986). Therefore, a

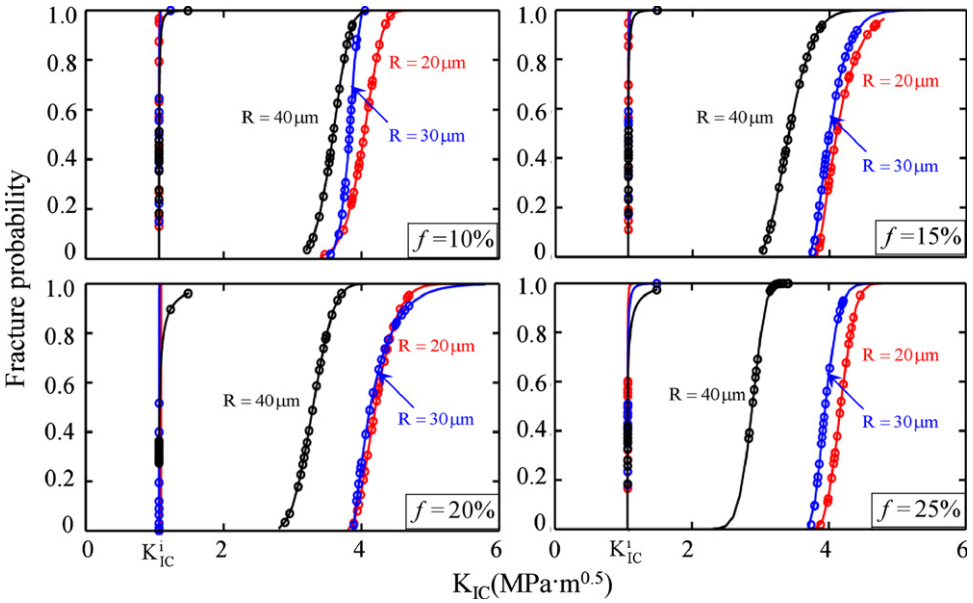

Fig. 11. Fracture probability distributions for microstructures with randomly distributed, non-overlapping circular reinforcement particles. The distributions are obtained from twenty random instantiations (samples) of each microstructure.

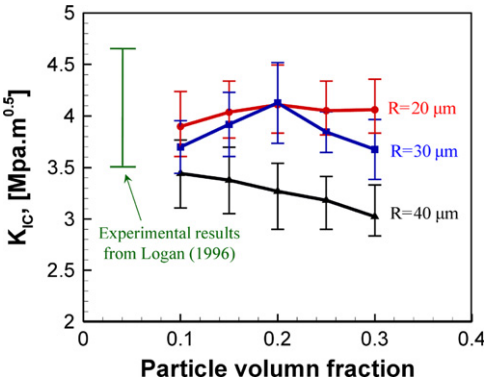

Fig. 12. Propagation toughness as a function of reinforcement size and volume fraction. The error bars indicate scatter of results obtained from twenty random instantiations (samples) of each microstructure.

probabilistic approach which accounts for microstructural morphology is needed. Fig. 14 shows the propagation toughness K^i_{IC} as a function of the two-point correlation parameter F_{01} measured at a crack propagation distance of $D=800$ μm. It can be seen that microstructures with finer reinforcements (higher values of F_{01}) have higher fracture toughness values due to their higher probability to cause crack arrest.

It is important to point out that so far we have only considered microstructures with perfectly circular particles. It is possible for different microstructures to have very similar two-point correlation functions. A case in point is shown in Fig. 15. The microstructures with elliptical, square and circular shaped reinforcement particles are generated from the real microstructure as listed in Fig. 8. All four microstructures have the same reinforcement volume fraction (15%), reinforcement orientation and size distribution. The nearly identical two-point correlation curves point to the need to quantify the effect of phase morphology or particle shape for particle-reinforced composites. Indeed, as we will discuss later, while the two-point correlation function measures the geometric probability for a crack to encounter the reinforcement, the shape parameter measures how the crack interacts with the reinforcement particles. Naturally, both aspects are important.

The mean reinforcement roundness $\overline{\rho}$ of a microstructure is defined as

$$\overline{\rho}=\frac{1}{n}\sum_{i=1}^{n}\rho^i=\frac{1}{n}\sum_{i=1}^{n}\frac{4A^i}{\pi(d^i_{\max})^2} \tag{15}$$

to quantify the circularity and surface irregularities of reinforcements in a microstructure (Russ, 2007; Seul, 2000; Valiveti and Ghosh, 2007). Here, A^i, $d^i_{\max}$ and ρ^i are the area, maximum distance and roundness of the ith reinforcement particle, respectively. n Is the total number of particles. Fig. 16 compares the distributions of the particle roundness values

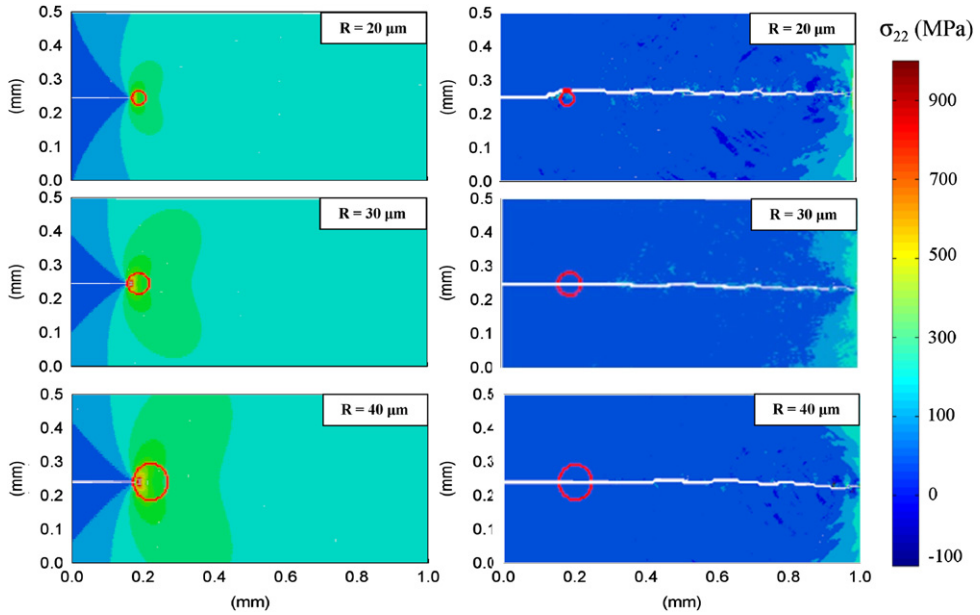

Fig. 13. The effect of reinforcement size on fracture mode.

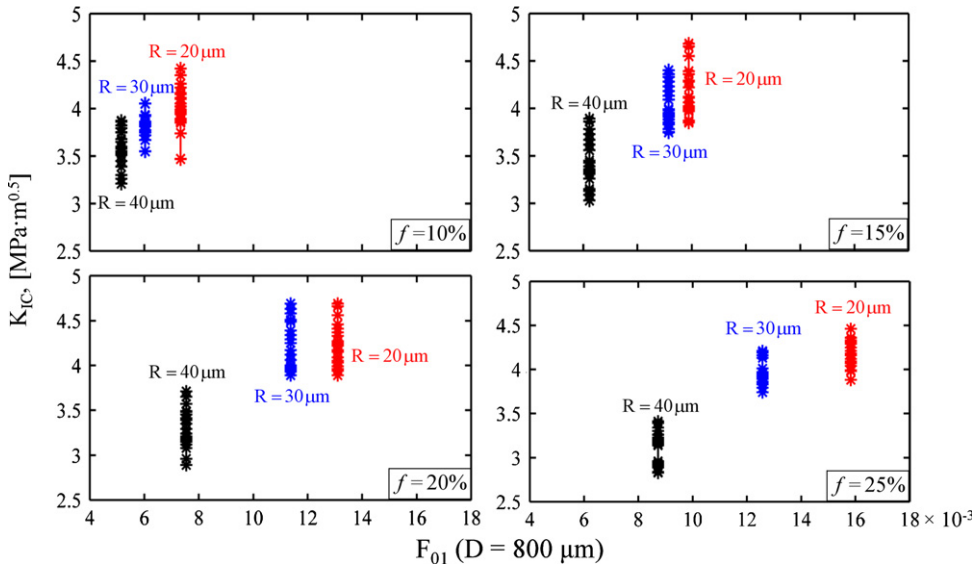

Fig. 14. Correlations between T_{max} and crack interaction parameter F_{01}. The scatter of results represents variations among twenty random instantiations (samples) of each microstructure.

of the four microstructures. The microstructure with elliptical reinforcement best approximates the real microstructure in terms of two-point correlation (Fig. 15) and particle morphology (Fig. 16). As a result, this microstructure has very similar K_{IC} values, as shown in Fig. 17. In contrast, the microstructures containing reinforcements with higher roundness values (circles and squares) show slightly different mean fracture toughness values. As we will see later, this is due to more extensive crack deflection associated with the higher-roundness microstructures.

4.3. *Effects of constituent attributes on fracture toughness*

The forgoing analyses show, from a morphological perspective, that particle cracking negatively influences fracture resistance, especially in the initial stage of crack–reinforcement interactions. It is equally important to identify the correlation between material attributes and the activation of fracture mechanisms. Here, we study the effects of

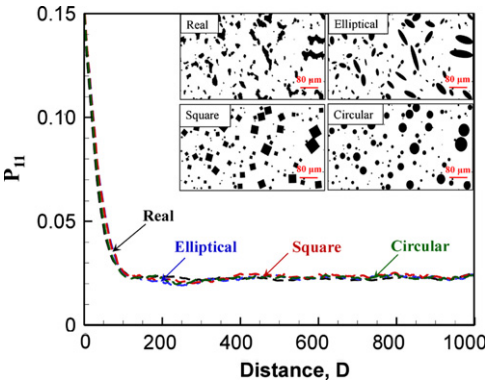

Fig. 15. Similarity between the two-point correlation functions of microstructures with different reinforcement particle shapes.

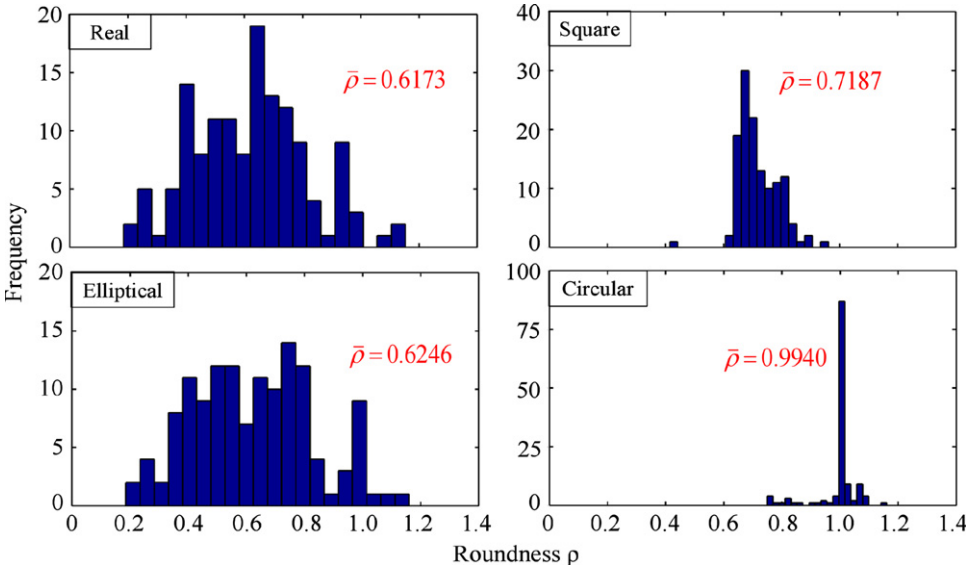

Fig. 16. Comparison of the roundness distributions for microstructures with different reinforcement shapes.

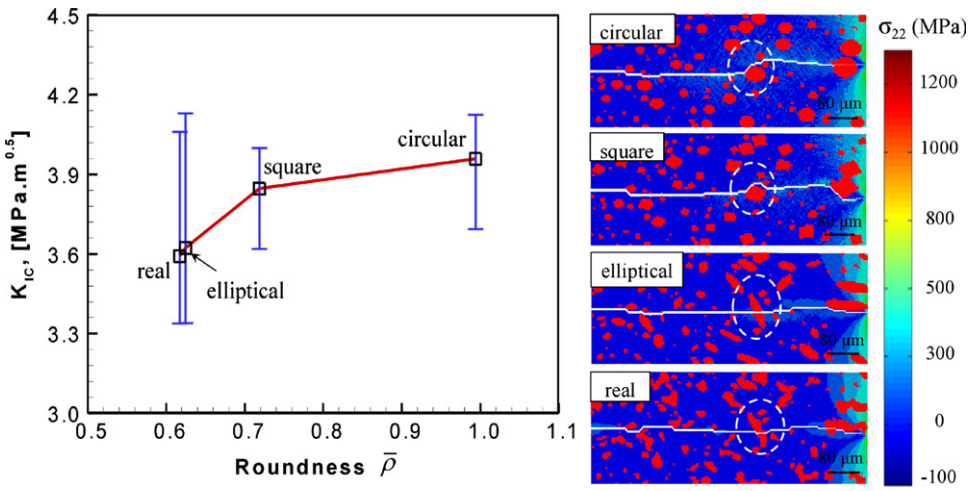

Fig. 17. Effect of mean roundness on K_{IC}. The error bars indicate scatter of results obtained from twenty random instantiations (samples) of each microstructure.

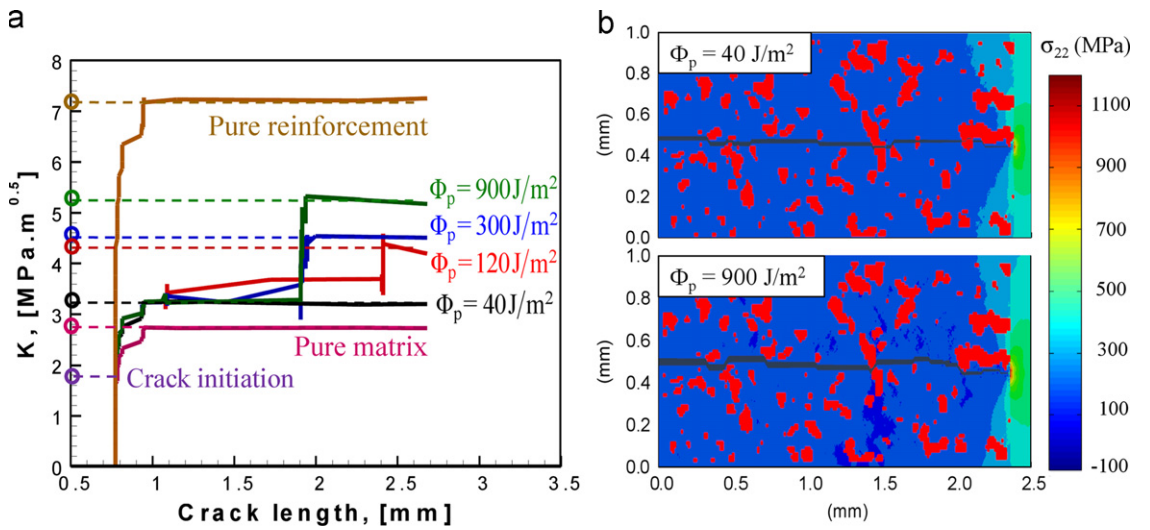

Fig. 18. Effect of reinforcement toughness on K_{IC}.

reinforcement toughness and compliance of the interface between the reinforcement phase and the matrix on fracture toughness.

Increasing the toughness of the reinforcement Φ_p has only a limited impact on the overall fracture toughness. It can be seen from Fig. 18(a) that the increase of fracture resistance tends to saturate beyond the Φ_p value of 120 J/m^2. Specifically, a 200% increase in Φ_p from 300 J/m^2 to 900 J/m^2 only leads to a 16% increase in K_{IC} from 4.4 MPa$\sqrt{\text{m}}$ to 5.2 MPa$\sqrt{\text{m}}$. In contrast, a 200% increase in Φ_p from 40 J/m^2 to 120 J/m^2 leads to an increase in K_{IC} of 31% from 3.2 MPa$\sqrt{\text{m}}$ to 4.2 MPa$\sqrt{\text{m}}$. A look at crack paths provides insight into this. Fig. 18(b) shows that particle cracking occurs even under unrealistically high Φ_p values, if the interfaces are well-bonded. Obviously, increasing Φ_p beyond a certain value has no significant impact on crack path, resulting in diminishing gains in K_{IC}.

On the other hand, interfacial bonding can significantly influence the dominant fracture mechanism and, consequently, alter the material fracture resistance. It has been proposed in some early studies (Evans, 1990; Mandell and McGarry, 1974) that under proper conditions, poor interface bonding could increase the fracture energy. A growing crack tends to meander along weakly bonded interfaces, leading to a tortuous crack trajectory. One way to address the role of interfacial bonding strength is to keep the interfacial fracture energy constant at Φ_{in}=78.5 J/m^2 and maintain the same slope of the initial linear portion of the cohesive relation (see Fig. 2) at 420 GPa. Under this condition, six different interfacial bonding strength levels ($T^{in}_{\max} = 6\times10^{-6}$, 6×10^{-4}, 6×10^{-3}, 6×10^{-2}, 0.6, and 6 GPa, corresponding to $Q_1 = T^{in}_{\max}/T^{0}_{\max} = 10^{-5}$, 10^{-3}, 10^{-2}, 10^{-1}, 1 and 10, respectively) are considered. Since the fracture energy is the same, the critical separations Δ_{tc} and Δ_{nc} are adjusted accordingly and the corresponding values are $\Delta_{tc}=\Delta_{nc}$=6800, 68, 6.8, 0.68, 0.068 and 0.0068 μm. These cases represent very compliant to very stiff interfaces. It should be noted that, as a rule of thumb, the interface is regarded as "well-bonded" if $T^{in}_{\max} \in [T^{m}_{\max}, T^{p}_{\max}] = [0.48, 0.7]$ GPa, where the K^0, $T^{m}_{\max}$ and $T^{p}_{\max}$ (Fig. 2) are the cohesive strengths of the interface, matrix and reinforcement, respectively, as listed in Table 1. Here for simplicity, we choose $T^{0}_{\max}$=0.6 GPa as the baseline case representing the well-bonded case. This baseline is the level used for calculations up to this point. The variations are considered relative to this baseline case. In particular, the case with $Q_1 = T^{in}_{\max}/T^{0}_{\max} = 10^{-5}$ essentially approximates a porous ceramic as though the particles do not exist.

The CFEM results in Fig. 19 and Fig. 20 show that the stiff interface (Q_1=10) leads to extensive particle cracking and a 14.7% decrease in K_{IC} relative to the baseline case (Q_1=1). As the bonding strength decreases (or interfacial compliance increases), more crack deflection into the matrix/reinforcement interfaces occurs, causing K_{IC} to increase initially, but ultimately decrease between $Q_1=10^{-3}$ and 10^{-5}. Particle cracking can be effectively avoided when the interfaces are quite compliant ($Q_1<1$). As Q_1 decreases, the interface becomes more ductile as interface debonding gradually outweighs matrix cracking and becomes the dominant fracture mode. It is noted that when $Q_1 = T^{in}_{\max}/T^{0}_{\max} = 10^{-5}$, the interfacial strength is negligibly small and the material essentially approximates porous ceramics as though the particles do not exist. This scenario is consistent with what has been reported for porous ceramics whose fracture toughness values are lower than two-phase or even single phase ceramics (Samborski and Sadowski, 2010). For $Q_1=10^{-3}$ the separation distance required for a complete decohesion of the cohesive elements along the interfaces can exceed the element size. This means that the interface may not fully debond and the damage at the interface cannot be considered as real cracks. However, the compliant interfaces serve as damage initiation sites. These damage sites contribute to energy dissipation and promote the formation of cracks in the matrix and the reinforcement. For complete debonding to occur at the interfaces, much larger microstructure samples than what is currently used and much longer load duration are needed. To simply put, the resulting energy released and fracture toughness value would be higher than what is shown in Fig. 20. With the

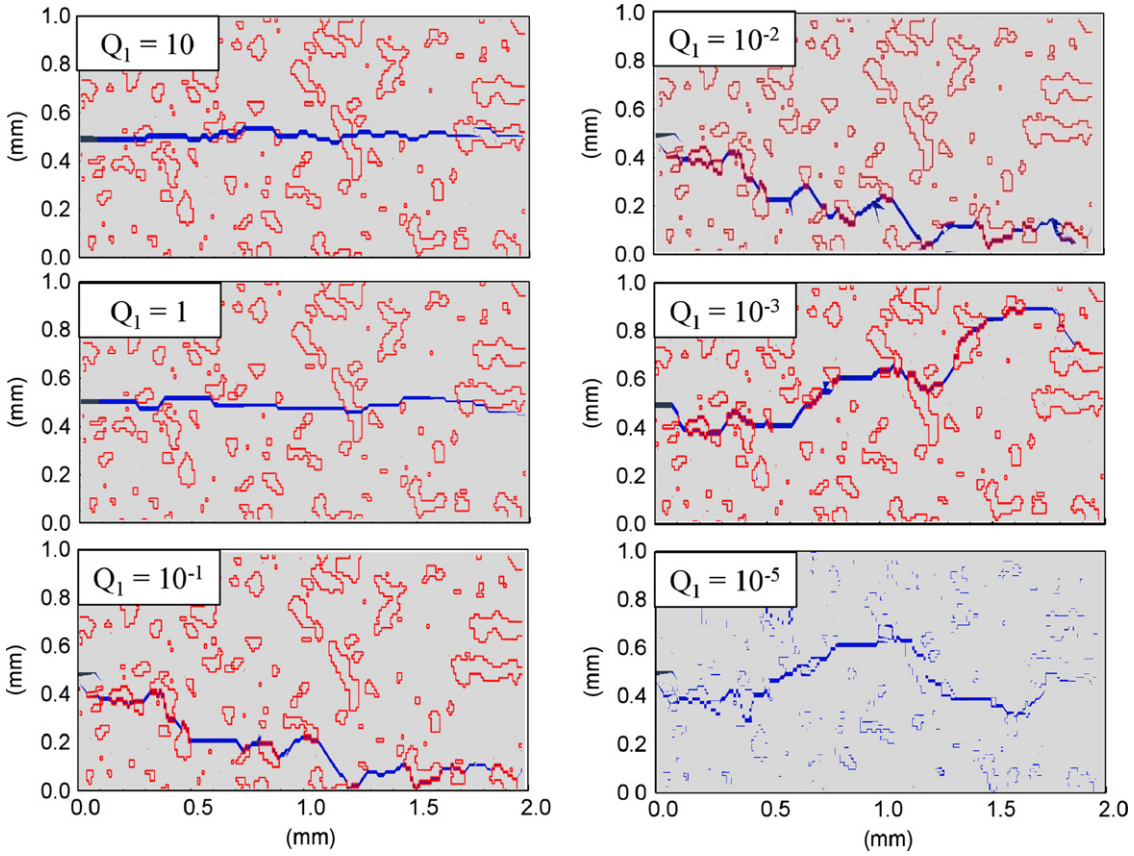

Fig. 19. Crack trajectories for different compliance or strength levels of the reinforcement–matrix interface as measured by the strength ratio Q_1.

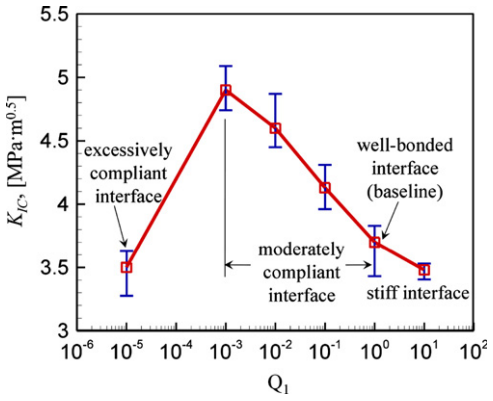

Fig. 20. Effect of compliance of the reinforcement–matrix interface as measured by the strength ratio Q_1 on K_{IC}. The error bars indicate scatter of results obtained from twenty random instantiations (samples) of each microstructure.

understanding that the K_{IC} value for $Q_1=10^{-3}$ in Fig. 20 being a conservative underestimate of the actual value, the trend of fracture toughness shown is valid and very illustrative. Specifically, to significantly improve the fracture resistance, the interfacial bonding between the matrix and particles of ceramic composites should balance strength and compliance. Excessively strong/stiff and overly weak or compliant interfaces are both detrimental. The data in Fig. 20 also show that increases of up to 50% in K_{IC} can be achieved by proper engineering of the interfacial bending strength/compliance, under the condition that the overall interfacial fracture energy is kept constant.

To illustrate the effect of bonding strength alone on K_{IC}, another set of calculations are carried out, with constant separation $\Delta_{tc}=\Delta_{nc}=0.068$ μm so as to keep the interfaces brittle and relatively non-compliant. Under this condition, six different interfacial bonding strength levels ($Q_2=T^{in}_{max}/T^0_{max}=10^{-5}$, 10^{-3}, 10^{-2}, 10^{-1}, 1 and 10, respectively, $T^0_{max}=0.6$ GPa, the same as before) are considered. These parameters guarantee full interface debonding for all the

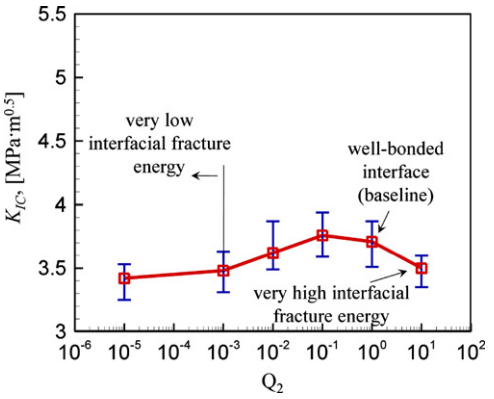

Fig. 21. Effect of bonding strength of the reinforcement–matrix interface as measured by the strength ratio Q_2 on K_{IC}. The error bars indicate scatter of results obtained from twenty random instantiations (samples) of each microstructure.

calculations under the conditions analyzed. Note that the cohesive energy changes for the six Q_2 levels while the initial slope of the cohesive relations remains constant at 420 GPa. As shown in Fig. 21, the trend of K_{IC} is similar to that in Fig. 20. However, the peak K_{IC} value occurs around $Q_2 \approx 10^{-1}$. Although lower Q_2 values promote crack deflection into the interface, the improvement in fracture toughness K_{IC} is very limited, as the fracture energy decreases dramatically when $Q_2 < 1$.

Noted that the K_{IC} value at $Q_2 = 10^{-5}$ is very close to the result shown in Fig. 20 when Q_1 is at the same value. This is due to the fact that interfacial bonding is essentially non-existent in both cases, effectively yielding a scenario in which the material is equivalent to a porous ceramic. Similarly, when $Q_2 = 10$, even though the fracture energy of the interface is 10 times that of the baseline case, K_{IC} is very similar to that in Fig. 20, due to the fact that interface debonding is completely replaced by particle cracking.

Obviously, the most effective way to improve fracture toughness is to create compliant (ductile) interfaces without sacrificing interfacial fracture energy. Fig. 20 shows that a proper balance must be maintained between interfacial bonding strength (or compliance) and the promotion of crack deflection. Excessively strong (or stiff) interfacial bonding increases penetration into particles and leads to catastrophic failure. Excessively weak (or compliant) bonding maximizes crack deflection but diminishes the toughening effect of the reinforcement. Both extremes result in lower fracture toughness values of the overall composite. A systematic quantification of the influences is important for materials design. A model to this effect is developed in Li and Zhou (in press) based on the computational results reported here.

5. Summary

A cohesive finite element method (CFEM) based multi-scale framework for analyzing the effects of microstructural heterogeneity, phase morphology, phase size, constituent behavior, and interfacial bonding strength on the fracture toughness of materials is developed. The computational framework allows the fracture initiation toughness and propagation toughness to be predicted as functions of microstructural attributes and constituent behavior. The method uses the *J*-integral and the linear elastic relation between *J* and *K*. The evaluation applies to steady-state crack propagation for which the driving force for fracture and fracture resistance of the material are in balance.

Calculations carried out concern Al_2O_3/TiB_2 two-phase ceramic composites and focus on the fundamental fracture mechanisms during crack initiation and propagation. Results of CFEM calculations show that both microstructure and constituent properties can significantly influence fracture behavior and combine to determine the overall fracture toughness through the activation of different fracture mechanisms. Interface debonding is the most beneficial fracture mechanism and is primarily promoted by small reinforcement size, rounded particle shapes and appropriately bonded and compliant reinforcement–matrix interfaces. In contrast, particle cracking, which triggers catastrophic material failure, usually occurs in microstructure with large reinforcement particles, lower particle roundness and over-bonded/stiff interfaces. Important constituent parameters are the fracture toughness of the matrix phase and the toughness of the interface between the matrix and the reinforcement phases. In contrast, increasing the toughness of the reinforcement phase beyond a certain level has only diminishing influence. CFEM calculations suggest a properly balanced level of interfacial bonding can maximize the fracture toughness of the materials if the interfacial fracture energy is kept constant as Φ_{in}. In the setting of this paper, $Q_1 = T^{in}_{max}/T^{0}_{max}$ values in the range of 10^{-3} to 10^{-2} offer an appropriate balance to maximize the propagation toughness of the Al_2O_3/TiB_2 material system.

The forgoing analyses point out that the fundamental avenue for toughening is the activation of different fracture mechanisms through the interplays between microstructure attributes which are stochastic on nature. To take advantage of the mechanisms, which can only be influenced in a statistical sense through microstructure design, it is important to quantify the relations between statistical measures for microstructure characteristics and statistical measures for the

fracture mechanisms. Such quantification can allow an analytical relation to be established between fracture toughness and microstructure. This will be the topic of Li and Zhou (in press).

Acknowledgment

This research is primarily supported by the NSF Center for Computational Materials Design (CCMD) at Georgia Institute of Technology and Pennsylvania State University. MZ also acknowledges support from the National Research Foundation of Korea through WCU Grant no. R31-2009-000–10083-0.

References

Anderson, T.L., 1995. Fracture Mechanics: Fundamentals and Applications. CRC Press, New York, US.
Berryman, J.G., Blair, S.C., 1986. Use of digital image analysis to estimate fluid permeability of porous materials: application of two-point correlation functions. J. Appl. Phys. 60, 1930.
Camacho, G.T., Ortiz, M., 1996. Computational modelling of impact damage in brittle materials. Int. J. Solids Struct. 33, 2899–2938.
Casellas, D., Nagl, M.M., Llanes, L., Anglada, M., 2003. Fracture toughness of alumina and ZTA ceramics: microstructural coarsening effects. J. Mater. Process. Technol. 143–144, 148–152.
Curry, D.A., Knott, J.F., 1976. The relationship between fracture toughness and microstructure in the cleavage fracture of mild steel. Met. Sci. 10, 1–6.
Doig, P., 1985. Evaluation of lower bound fracture-toughness values using Weibull analysis of single specimen data. Eng. Fract. Mech. 21, 963–967.
Duffy, J., Suresh, S., Cho, K., Bopp, E.R., 1988. A method for dynamic fracture initiation testing of ceramics. J. Eng. Mater. Technol. 110, 325–331.
Espinosa, H.D., Dwivedi, S., Lu, H.C., 2000. Modeling impact induced delamination of woven fiber reinforced composites with contact/cohesive laws. Comput. Method Appl. Mech. 183, 259–290.
Evans, A.G., 1990. Perspective on the development of high-toughness ceramics. J. Am. Ceram. Soc. 73, 187–206.
Freund, L.B., 1998. Dynamic Fracture Mechanics. Cambridge University Press, Cambridge, UK.
Hall, J.N., Jones, J.W., Sachdev, A.K., 1994. Particle-size, volume fraction and matrix strength effects on fatigue behavior and particle fracture in 2124 Aluminum-Sicp composites. Mater. Sci. Eng. A 183, 69–80.
Kobayashi, A.S., Ramulu, M., Dadkhah, M.S., Yang, K.H., Kang, B.S.J., 1986. Dynamic fracture toughness. Int. J. Fract. 30, 275–285.
Kumai, S., King, J.E., Knott, J.F., 1991. Fatigue in Sic-particulate-reinforced Aluminum-alloy composites. Mater. Sci. Eng. A 146, 317–326.
Li, Y., Zhou, M. Prediction of fracture toughness of ceramic composites as a function of microstructure: II. Analytical model. J. Mech. Phys. Solids, http://dx.doi.org/10.1016/j.jmps.2012.09.011, in press.
Lin, T., Evans, A.G., Ritchie, R.O., 1986. Statistical analysis of cleavage fracture ahead of sharp cracks and rounded notches. Acta Metall. Mater. 34, 2205–2216.
Lo, C.Y., Nakamura, T., 1993. Computational analysis of dynamically propagating cracks in axisymmetric solids. Int. J. Fract. 70, 217–235.
Logan, K.V., 1996. Composite Ceramics, Final Technical Report. USSTACOM DAAEO7-95-C-R040.
Mandell, J.F.M.G.B., McGarry, F.J., 1974. Interlaminar Strength and Toughness of Fiberglass Laminates. The Society of the Plastics Industry, Inc., Washington, D.C. (13-C).
Manoharan, M., Kamat, S.V., 1993. A micro-mechanical model for crack growth resistance of particulate-reinforced metal–matrix composites. J. Mater. Sci. 28, 5218–5222.
Moran, B., Shih, C.F., 1987. A general treatment of crack tip contour integrals. Int. J. Fract. 35, 295–310.
Nakamura, T., Shih, C.F., Freund, L.B., 1985. Computational methods based on an energy integral in dynamic fracture. Int. J. Fract. 27, 229–243.
Needleman, A., 1990. An analysis of tensile decohesion along an interface. J. Mech. Phys. Solids 38, 289–324.
Ortiz, M., Pandolfi, A., 1999. Finite-deformation irreversible cohesive elements for three-dimensional crack-propagation analysis. Int. J. Numer. Methods Eng. 44, 1267–1282.
Pandolfi, A., Ortiz, M., 2002. An efficient adaptive procedure for three-dimensional fragmentation simulations. Eng. Comput. 18, 148–159.
Russ, J.C., 2007. The Image Processing Handbook. CRC Press, New York, US.
Samborski, S., Sadowski, T., 2010. Dynamic fracture toughness of porous ceramics rapid communications of the American Ceramic Society. J. Am. Ceram. Soc. 93, 3607–3609.
Seul, M., 2000. Practical Algorithms for Image Analysis: Description, Examples, and Code. Cambridge University Press, Cambridge, MA (O.G.L.S.M.J.).
Tewari, A., Gokhale, A.M., Spowart, J.E., Miracle, D.B., 2004. Quantitative characterization of spatial clustering in three-dimensional microstructures using two-point correlation functions. Acta Metall. Mater. 52, 307–319.
Tomar, V., Zhai, J., Zhou, M., 2004. Bounds for element size in a variable stiffness cohesive finite element model. Int. J. Numer. Methods Eng. 61, 1894–1920.
Torquato, S., Haslach Jr., H.W., 2002. Random heterogeneous materials: microstructure and macroscopic properties. Appl. Mech. Rev. 55, B62–B63.
Toshiro, K., Kenji, M., Hideki, I., Kenya, M., 1988. Evaluation of static and dynamic fracture toughness in ceramics. Eng. Fract. Mech. 31, 873–885.
Valiveti, D.M., Ghosh, S., 2007. Morphology based domain partitioning of multi-phase materials: a preprocessor for multi-scale modelling. Int. J. Numer. Methods Eng. 69, 1717–1754.
Wallin, K., 1984. The scatter in K_{IC}—results. Eng. Fract. Mech. 19, 1085–1093.
Wallin, K., 1993. Macroscopic nature of brittle fracture. J. Phys. IV 3 (IV), 575–584. (Colloque C7, Supplément au J Phys III).
Wallin, K., Törrönen, K., Ahlstrand, R., Timofeev, B., Rybin, V., Nikolaev, V., Morozov, A., 1992. Theory based statistical interpretation of brittle fracture toughness of reactor pressure vessel steel 15X2MφA and its welds. Nucl. Eng. Des. 135, 239–246.
Weibull, W., 1939. A statistical theory of the strength of materials. Ing. Vetenskaps. Akad. Handl. 151, 1–45.
Wiederhorn, S.M., 1984. Brittle-fracture and toughening mechanisms in ceramics. Annu. Rev. Mater. Sci. 14, 373–403.
Xu, X.P., Needleman, A., 1985. Numerical simulations of dynamic interfacial crack growth allowing for crack growth away from the bond line. Int. J. Fract. 74, 253–275.
Xu, X.P., Needleman, A., 1994. Numerical simulations of fast crack-growth in brittle solids. J. Mech. Phys. Solids 42, 1397.
Yu, C., 2001. Three-Dimensional Cohesive Modeling of Impact Damage of Composites. Caltech, Pasadena, CA.
Zhai, J., Tomar, V., Zhou, M., 2004. Micromechanical simulation of dynamic fracture using the cohesive finite element method. J. Eng. Mater. Technol. 126, 179–191.
Zohdi, T.I., Wriggers, P., 2008. An Introduction to Computational Micromechanics. Springer-Verlag GmbH, Germany.